Microstructure and Crystallographic Texture in Twin-Roll Casting of AA1050 Aluminum Alloy: Simulation and Industrial Validation

JONATHAN DANTZIG, ONUR MEYDANOĞLU, ARASH KAZAZI, HATİCE MOLLAOĞLU ALTUNER, CEMİL IŞIKSAÇAN, and MELİS ŞEREFOĞLU

Twin-roll casting (TRC) is a process in which liquid metal is introduced directly between counter-rotating water-cooled rolls, where it solidifies and is rolled to a strip having final thickness of 3 to 8 mm. TRC for aluminum is best suited to those alloys having a narrow freezing range with little susceptibility to hot tearing, such as 1XXX, 3XXX, 5XXX, and 8XXX. TRC offers advantages over conventional DC casting followed by hot and cold rolling for these alloys due to its lower capital cost, and decreased downstream processing operational cost and energy consumption, since hot rolling is not required. The microstructure formed in the strip must be carefully controlled, because as a near-net shape product used mostly for non-age-hardenable alloys, there is limited opportunity to modify it by subsequent processing. In particular, the near-surface microstructure has a strong effect on performance in forming applications. In this article, we present a computational model of TRC, and validate it for AA1050 aluminum alloy in a production environment. The novel aspect of this work is that the model is used to predict the final microstructure and crystallographic texture of the cast strip. The model is validated in plant trials for strip cast at a range of thicknesses, casting speeds, and caster setup by comparing the predicted microstructure, texture, and process outcomes such as roll separating force and forward slip to their corresponding measured values. We then apply the validated model to explore process parameters outside the standard practices, including feed inlet setback, casting speed, metal inlet temperature, and changing roll material to demonstrate how the microstructure and texture can be controlled via these parameters.

I. INTRODUCTION

THE twin-roll casting (TRC) process has been an important industrial production process for aluminum alloys for more than 50 years. Liquid alloy is introduced through a ceramic inlet between two counter-rotating rolls in either a near-horizontal or vertical configuration. The metal freezes near the inlet, and is then rolled to a final thickness between 3 and 8 mm. Cast strips are typically about 2 m wide. The rolls consist of cylindrical shells made of steel or Cu, mounted on a water-cooled core. A mold release agent is provided to prevent adhesion between the strip and rolls, in the form of a colloidal graphite suspension, sprayed directly onto the rolls. The roll shells are subject to thermal and mechanical fatigue cracking, and are periodically removed for surface grinding before being put back into service.

The aluminum alloys most commonly produced by TRC are those with a relatively narrow freezing range, and little susceptibility to hot tearing. These include the 1XXX, 3XXX, 5XXX, and 8XXX alloys. The cast strip often receives an annealing treatment in order to improve its formability. The as-cast strip microstructure, especially near the surfaces, strongly affects the annealing response. In particular, a strong shear texture and highly deformed grains tend to produce excessive grain growth during annealing, which may lead to poor performance in subsequent forming operations. The ideal cast microstructure would consist of uniform equiaxed grains, especially near the surface of the strip.

Numerous models of the TRC process have appeared in the literature to predict the temperature and velocity fields in the cast strip, usually validated by comparison

JONATHAN DANTZIG is with the Department of Mechanical Science and Engineering, University of Illinois, 1206 West Green Street, Urbana, IL 61801. Contact e-mail: dantzig@illinois.edu ONUR MEYDANOĞLU, HATİCE MOLLAOĞLU ALTUNER, and CEMİL IŞIKSAÇAN are with the Assan Aluminum, Yayla Mh. D-100, Karayolu Rüya Sk. No.2, 34940 Tuzla, Istanbul, Turkey. ARASH KAZAZI is with the Department of Mechanical Engineering, Koc University, Rumeli Feneri Yolu, 34450 Sariyer, Istanbul, Turkey. MELİS ŞEREFOĞLU is with the Department of Metallurgical and Materials Engineering, Marmara University, Aydinevler Mah., 34854 Maltepe, Istanbul, Turkey

Manuscript submitted April 25, 2022; accepted August 29, 2022.

Published online: 14 October 2022

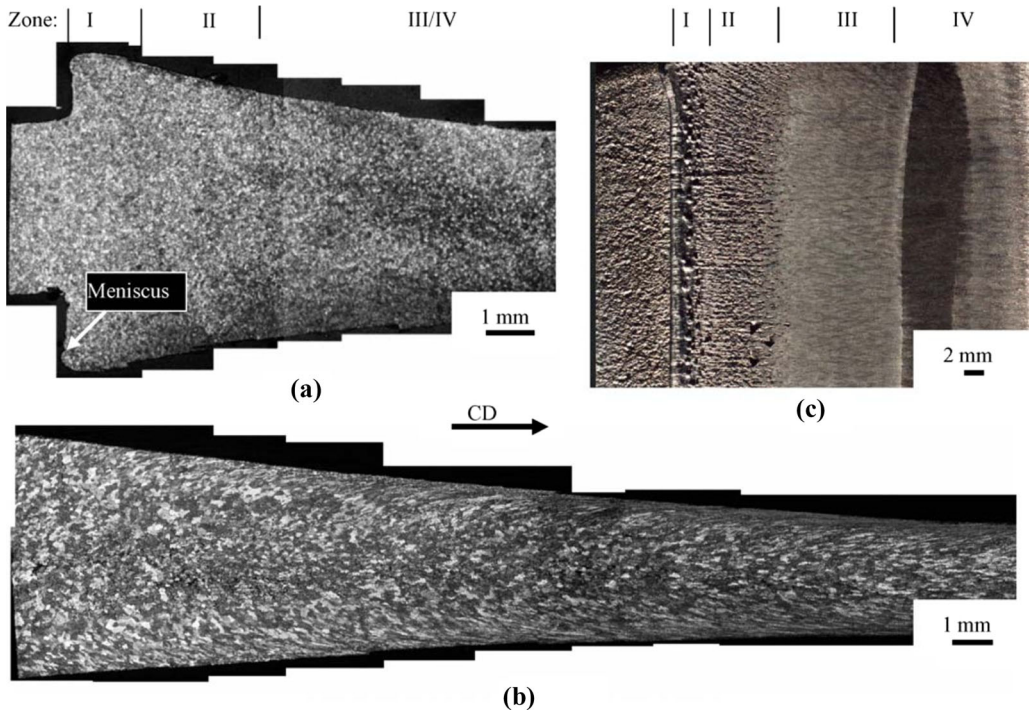

Fig. 1—Stop-samples from AA5052 in a pilot TRC caster. Longitudinal sections of (*a*) 4.1-mm-thick strip cast at 25 mm/s; (*b*) 2.0-mm-thick strip cast at 93 mm/s. (*c*) Top surface of the 4.1 mm strip. Reprinted with permission from Forbord *et al.*[1].

to extrinsic measures such as roll separating force and forward slip. We describe some of these works further below, before presenting a similar model of our own.

The features of the process and microstructure that are important to capture in the model can be understood with the help of Figures 1(a) and (b), reprinted from Forbord *et al.*,[1] which show longitudinal microstructures of stop-samples of AA5052 strip cast at two different speeds and gages. Figure 1(c) shows the top surface of Sample (a) after solidification.

The longitudinal micrographs show that the highly grain-refined alloy solidifies initially as equiaxed crystals in both samples. Sample (a), which was thicker and cast at relatively low speed, remains nearly equiaxed, whereas Sample (b) exhibits highly deformed grains near the surface that become increasingly elongated with distance along the roll. This demonstrates that casting conditions have a very significant effect on the cast microstructure, and that the surface grain structure is a result of post-solidification deformation. The work that we present in this article focuses on the deformation-induced microstructure in the strip.

Figure 1(c) shows the top surface of Sample (a), for which Forbord *et al.* identified four regions: Region I was associated with the meniscus formed between the inlet and roll, before initial contact. Region II corresponds to the first contact with the roll, and the corrugations in the surface correspond to solidification shrinkage. In Region III, the surface protrusions found in Region II were found to be bent toward the casting direction, and in Region IV those protrusions were completely flattened. We will capture the observed phenomena in Regions II–IV in our model *via* a pressure-dependent heat transfer coefficient, rising from a low value during the initial stage of solidification when the strip is unable to support much pressure to a high value associated with the heavily deformed Regions III and IV. Further details will be given in Section II–B.

We begin with a brief review of previous work to model TRC. Roadman *et al.*[2] presented a model in 1982 that has nearly all of the features included in virtually all of the models published since then: The strip and rolls are modeled as a 2-D longitudinal section, assumed to be in plane strain, using the finite element method (FEM). The cast strip is modeled as a viscous fluid above a specified coherency temperature, and a viscoplastic solid below that temperature. Roadman *et al.* identified as key controlling parameters the heat and mechanical transport properties at the roll–strip interface. They modeled the heat transfer *via* a pressure-dependent heat transfer coefficient, and the interfacial shear stress as proportional to the difference between the roll and strip surface speeds. The specific values for these parameters were not included in their article. They used measured values of roll torque, roll separating force, and strip exit temperature to calibrate their model. Subsequent modeling efforts by numerous authors are built upon this work and extended in several ways. Sahoo[3] provided a review for applications to vertical TRC. We provide here a limited discussion of the literature that is most applicable to our work.

Several authors have attempted to measure the heat transfer coefficient as a function of roll pressure.[4,5] Jarry *et al.*[6] presented a model for an industrial Jumbo 3C caster that represented the roll–strip heat transfer coefficient as rising from a minimum value of 10 to 25

kW/m^{2}K at low contact pressure, to a maximum of 100 kW/m^{2}K at high contact pressure. We will adopt a similar model in the work described below. They also included a pressure-dependent friction coefficient for the roll–strip interface. We will use a constant value for this parameter. Their model was able to predict strip surface defects that appear under some casting conditions.

Hwang and Kang[7] modeled a vertical TRC configuration, focusing on the fluid flow in the initial region of solidification, and its role in determining the solidification behavior of the cast strip. Sahoo *et al.*[8] also modeled a vertical TRC caster, including a turbulence model for the flow in the liquid. To validate their model, they cast an Al-33 wt pct Cu alloy, and used well-known correlations between the eutectic lamellar spacing and solidification conditions to calibrate the (constant) heat transfer coefficient used in the model. This is one of the very few instances where the strip microstructure was used as part of the model validation process. Lee *et al.*[9,10] build a pilot-scale caster with instrumented rolls, which they used in conjunction with a model to estimate the heat transfer coefficient between the strip and rolls to be 6.5 to 10 kW/m^{2}K. The model was applied to AA7075 alloy, and the roll separating force was used as a measure of the fidelity of the model.

Mortensen *et al.*[11] implemented a combined Eulerian and Arbitrary Lagrangian Eulerian method to represent different parts of the strip and rolls. They also included as part of the strip a meniscus that forms between the end of the ceramic inlet and the rolls. The strip–roll heat transfer was adjusted in an unspecified manner in order to match the strip exit temperature, roll separating force, and forward slip. More recently, Grydin *et al.*[12] used an instrumented lab-scale vertical TRC caster in conjunction with a numerical model to estimate the strip–roll heat transfer coefficients that ranged from 15 to 65 kW/m^{2}K as a function of arc length along the roll.

Rodrigues *et al.*[13,14] added micro-modeling of nucleation and growth, as well as phase separation in the deforming mush to examine segregation in TRC of an Al-4 wt pct Cu alloy. The nucleation model predicts a fine-grained equiaxed microstructure at the coherency point, which we will use as the initial microstructure when we examine the deformation-induced microstructure and texture in the final strip.

There have also been a few studies of the microstructure and texture in TRC. Gras *et al.*[15] characterized the texture in TRC strip as having an outer zone with a shear texture, and a central core with a typical plane strain compression texture. The depth of penetration of the shear zone into the strip is important for TRC, because it directly affects the grain structure after heat treatment.[16] Jung *et al.*[17] showed for conventional rolling that the plane strain compression texture rotates opposite to the rolling direction as one goes from the center toward the surface, before reaching the surface shear zone. One of our goals is to predict the texture through the strip thickness.

We built upon this body of literature to develop a model of the TRC process. The novel aspect of our work is the ability to predict quantitatively the microstructure and crystalline texture in the cast strip. The model is validated *via* measurements on AA1050 aluminum alloy cast in industrial production. After validating the model, we explore ways to control the internal structure via modification of processing parameters. The rest of this article is organized as follows: We first briefly present the computational model for temperature and velocity in the strip, followed by a description of the methods for prediction of the microstructure and texture used to compare and validate the model predictions. We train the model using 5.13-mm-thick AA1050 strip taken from a production run, to determine the strip–roll interface transport parameters. We then validate the model by applying it to a different production run in which several different strip thicknesses were produced under varying processing conditions. The validated model is then used to explore processing conditions to alter and control the microstructure and crystallographic texture.

II. TRC MODEL

In the plant operations that we aim to model, the cast Al strip is typically 3 to 6 mm thick and about 2.2 m wide. This geometry makes it appropriate to model the process in 2-D, and to treat the 2-D section as being in plane strain. We describe later a way to extend the model in the cross-strip direction to account for the contribution to the total separating force of thickness variation due to roll flattening/crowning.

The model domain is shown schematically in Figure 2, identifying several of the parameters that are used to define the geometry and boundary conditions. The liquid alloy is introduced at a specified temperature on the left side, passes through an inlet (not included in the model), which is offset horizontally from the roll nip, and may also be offset vertically with respect to the centerline of the caster. The inlet is narrower than the opening between the rolls, and thus the liquid forms a meniscus as it expands to fill the gap (see Figure 1(c)). The length Lx_{free} and radius of curvature R_{free} for this free surface region are input parameters. Although the true physical values of these two parameters are not known precisely, the microstructure calculations that are the focus of our work turn out not to be very sensitive to their exact values. The boundary conditions on the various surfaces are given in Table I.

The temperature distribution in the rolls is also computed as part of the solution. Figure 3 shows a

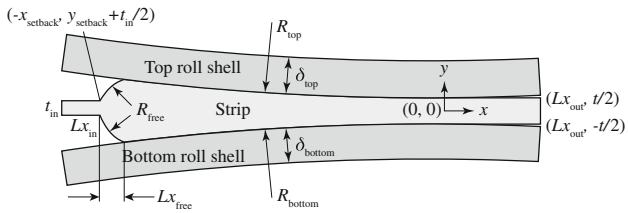

Fig. 2—Schematic representation of the domain of the model. The roll shells are much thicker than illustrated here.

Table I. Boundary Conditions (BC) at the Various Surfaces in the Model

Surface	Velocity BC	Heat Flux BC
Inlet Left	$\partial \mathbf{v}/\partial n = 0$	0
Inlet Top & Bottom	$v_n = 0$	0
Meniscus	$v_n = 0$	0
Outlet Top & Bottom	$v_n = 0$	$h_{out}(T - T_\infty^{out})$
Outlet Right	$\partial \mathbf{v}/\partial n = 0$	0
Top Inner Shell R_i^t	$v_t = \Omega_t R_i^t,\ v_n = 0$	$h_w(T - T_w)$
Bottom Inner Shell R_i^b	$v_t = \Omega_b R_i^b,\ v_n = 0$	$h_w(T - T_w)$
Strip–roll Interface	$\tau_{r\theta} = \beta(\mathbf{v}_{roll} - \mathbf{v}_{strip}) \cdot \hat{\mathbf{t}}$ $v_n = 0$	$\pm h(p)[T_{roll} - T_{strip}]$

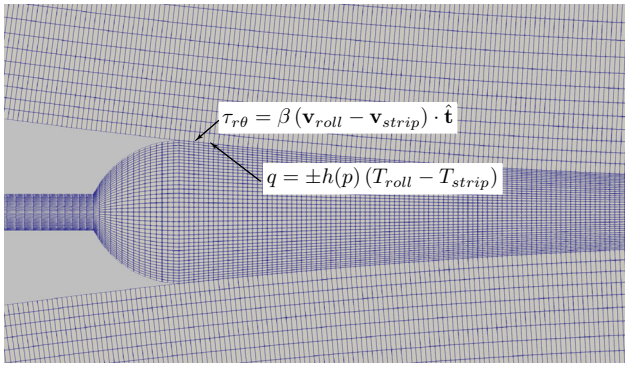

Fig. 3—Detail of the mesh near the interface between the strip and the roll, along with boundary conditions.

detail of the mesh and boundary conditions near the strip–roll interface. Heat transport at the inner radius of the roll shells is modeled with a heat transfer coefficient h_w and the supplied water temperature T_w. See Table I. The heat flux q between the strip and rolls is mediated by a pressure-dependent heat transfer coefficient $h(p)$, described further in Section II–B:

$$q = \pm h(p)\left(T_{\text{roll}} - T_{\text{strip}}\right), \qquad [1]$$

where the "+" sign corresponds to computing temperature in the strip, and the "−" sign applies to computing temperature in the roll shells. Following Roadman *et al.*[2] and Harnish *et al.*,[18] the shear stress in the strip at the roll surface is modeled as being proportional to the difference in tangential speed between the roll and the strip.

$$\tau_{r\theta} = \beta\left(\mathbf{v}_{\text{roll}} - \mathbf{v}_{\text{strip}}\right) \cdot \hat{t}, \qquad [2]$$

where β is called the *slip coefficient* and $\hat{\boldsymbol{t}}$ is the local tangent vector.

The temperature and velocity fields in the strip and rolls are assumed to be steady and two-dimensional. For the strip, we have

$$\nabla \cdot \mathbf{v} = 0 \qquad [3]$$

$$\rho \mathbf{v} \cdot \nabla \mathbf{v} = -\nabla p + \nabla \cdot (\eta(g_s, T, \dot{\varepsilon}) \nabla \mathbf{v}) \qquad [4]$$

$$\rho C_p(T) \mathbf{v} \cdot \nabla \mathbf{T} = \nabla \cdot (k \nabla T) + 2\eta(\mathbf{D} : \mathbf{D}), \qquad [5]$$

where $\mathbf{v}$ is the velocity, ρ is the density, $\eta(g_s, T, \dot{\varepsilon})$ is the non-Newtonian viscosity that depends on the solid fraction g_s, temperature T, and strain rate $\dot{\varepsilon} = \sqrt{(2/3)\mathbf{D} : \mathbf{D}}$, where $\mathbf{D} = (1/2)(\nabla \mathbf{v} + \nabla \mathbf{v}^{\mathbf{T}})$ is the rate of deformation tensor. The energy balance, Eq. [5], contains the temperature-dependent specific heat $C_p(T)$ to be defined further in Section II–A–1, the thermal conductivity k, assumed to be constant, and the final term on the right-hand side is the viscous dissipation.

The governing equations in the rolls are somewhat simpler than those in the strip because the velocity field is known:

$$\mathbf{v}_{\text{roll}} = r\Omega_{\text{roll}}\hat{\boldsymbol{\theta}}, \qquad [6]$$

where r is the radial distance from the roll center, Ω_{roll} is the angular velocity of the top or bottom roll, and $\hat{\boldsymbol{\theta}}$ is the unit vector perpendicular to the radius. There is no viscous dissipation in the rolls. The energy equation in the roll is given by

$$\rho\, C_p^{\text{roll}} v_{\text{roll}} \cdot \nabla T = \nabla \cdot (k_{\text{roll}} \nabla T). \qquad [7]$$

A. *Material Properties*

1. *Enthalpy, solid fraction, and specific heat*

The model takes as input an Enthalpy–Temperature (H–T) curve, which is determined experimentally using differential scanning calorimetry (DSC) on the AA1050 alloy used in production at Assan Aluminum. The DSC also gives the solid fraction as a function of temperature, $g_s(T) = 1 - g_\ell(T)$. The solid fraction and enthalpy are related through the latent heat of fusion L_f and specific heats of the solid and liquid phases c_p^s and c_p^ℓ, respectively,

$$H = H(T_0) + \int_{T_0}^{T} c_p(g_s)dT + L_f(1 - g_s), \qquad [8]$$

where T_0 is an arbitrary reference temperature, and $c_p(g_s) = c_p^s g_s + c_p^\ell(1 - g_s)$. In the FEM implementation, the effective specific heat $C_p(T)$ is computed at each integration point from the local temperature field as[19]

$$C_p(T) = \left(\frac{\nabla H \cdot \nabla H}{\nabla T \cdot \nabla T}\right)^{1/2}. \qquad [9]$$

To aid in convergence of the computations, the liquid fraction curve is modified from the one derived from the DSC measurements. AA1050 has a very narrow freezing range, and hence the slope of the $g_\ell - T$ curve changes

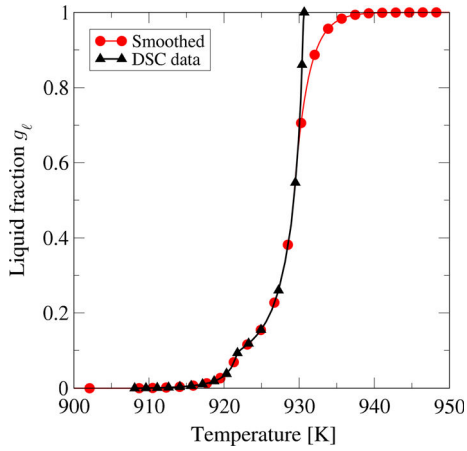

Fig. 4—Liquid fraction $g_\ell = 1 - g_s$ *vs.* temperature curve as measured by DSC (black triangles) and modified for improved convergence (red circles) (Color figure online).

very sharply near the liquidus, which can lead to convergence problems in the calculations. Since the details of this part of the temperature field are of less interest in this work, the curve used is smoothed near the liquidus, as shown in Figure 4.

2. *Non-Newtonian viscosity* $\eta(g_s, T, \dot{\varepsilon})$

The mechanical behavior of the strip is modeled as a non-Newtonian viscous fluid, having two distinct regions according to the solid fraction g_s. Following the model of Rodrigues *et al.*,[13,14] we define a coherency solid fraction as $g_s^t = 0.57$. Above the liquidus temperature, *i.e.*, when $g_s = 0$, the viscosity is that of the liquid, μ_ℓ. For $0 < g_s \leq g_s^t$, the viscosity increases with increasing g_s as a power law. In equation form, these two regions are combined into one equation, given by

$$\eta = \frac{\mu_\ell}{g_s}\left[\left(1 - \frac{g_s}{g_s^p}\right)^{-2.5 g_s^p} - (1 - g_s)\right] \quad 0 \leq g_s \leq g_s^t, \quad [10]$$

where $g_s^p = 0.585$ is a normalizing factor.[13,14]

Above the coherency solid fraction, $g_s > g_s^t$, the material is treated as a viscoplastic solid. The saturation stress σ_{sat} is written as a function of the Zener–Holloman parameter Z, also called the temperature-compensated strain rate, given by

$$Z = \dot{\varepsilon} \exp\left(\frac{Q_D}{\mathcal{R}T}\right), \quad [11]$$

where Q_D is an activation energy for diffusion and $\mathcal{R}$ is the ideal gas constant. The saturation stress σ_{sat} is obtained from the correlations given by Sheppard and Jackson for AA1050[20]

$$\sigma_{sat} = \frac{1}{\alpha}\ln\left(\left[\left\{\frac{Z}{A}\right\}^{1/n} + \left(1 + \left\{\frac{Z}{A}\right\}^{2/n}\right)^{1/2}\right]\right), \quad [12]$$

where α, A, and n are material parameters tabulated in Reference 20 for various Al alloys. The values used here are given in Table II. Please note that whereas Sheppard and Jackson gives a value of $Q_D = 156.888$ kJ/mol, we found through numerical experimentation that $Q_D = 150$ kJ/mol gave a better fit to the production data for separating force. The other parameters were unchanged from those given by Sheppard and Jackson. The non-Newtonian viscosity $\eta(Z)$ for $g_s \geq g_s^t$ is then computed as $\eta(Z) = \sigma_{sat}/3\dot{\varepsilon}$. An example of the composite viscosity as a function of temperature at various strain rates for AA 1050 is shown in Figure 5(a).

Table II. Parameters Used in the Simulations

Viscoplastic Model Parameters[20]	
α^{-1}[MPa]	27.03
A [s^{-1}]	3.9×10^{11}
n [–]	3.84
Q_D [kJ/mol]	150
Roll–Strip Heat Transfer Model Parameters	
h_{min}[kW/m^{2}K]	7.5-9.5
h_{max} [kW/m^{2}K]	100
P_{mid} [MPa]	13
P_{width} [MPa]	3

B. *Heat Transfer Coefficient*

We generalize the model for $h(p)$ given by Jarry *et al.*[6] to provide a smooth transition between the regions of low and high heat transfer. Our model has four parameters $(h_{\text{min}}, h_{\text{max}}, P_{\text{mid}}, P_{\text{width}})$, satisfying

$$h = h_{\text{min}} + 0.5(h_{\text{max}} - h_{\text{min}})(1 + \tanh[(p - P_{\text{mid}})/P_{\text{width}}]). \quad [13]$$

The values for these parameters used in the simulations presented in the following sections are given in Table II, and plotted in Figure 5(b).

III. IMPLEMENTATION

The governing equations are solved using the finite element method, implemented in a code written specifically for TRC using MATLAB.[21] The formation of element matrices and force vectors follow the usual Galerkin procedure, and are omitted here. The advective terms in both the momentum and energy balance equations for the strip are stabilized by using the Streamline Upwind Petrov–Galerkin (SUPG) method of Brooks and Hughes.[22] The mesh consists of 4-noded isoparametric quadrilaterals, using linear interpolation for velocity and temperature, and piecewise constant pressure (Stabilized Q1P0 elements).

The governing equations for the velocity and temperature fields are coupled and highly non-linear, due to the essentially exponential variation with temperature of the viscosity, specific heat, and strip–roll heat transfer boundary condition. For this reason, they are solved iteratively and in sequence. The solution algorithm

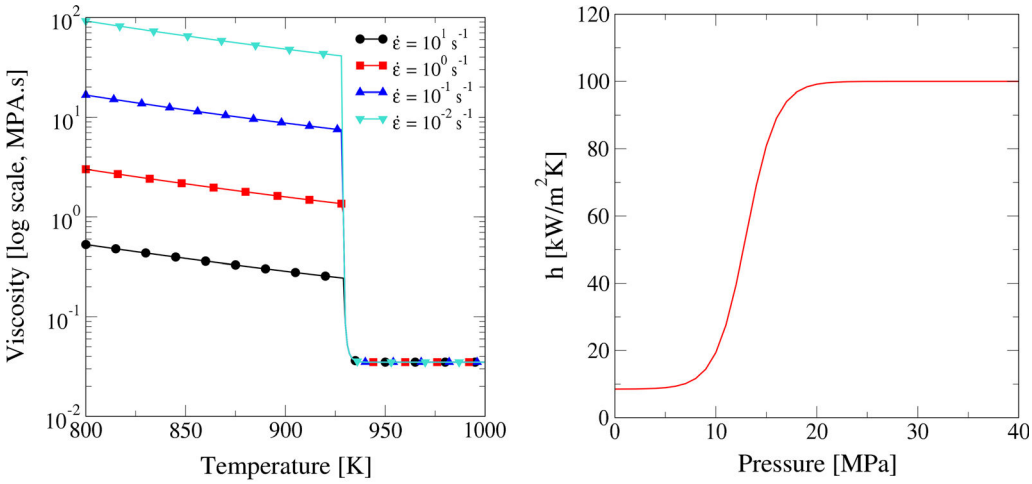

(a) Non-Newtonian viscosity **(b)** Heat transfer coefficient

Fig. 5—(*a*) Viscosity of AA1050 as a function of temperature for several different strain rates. (*b*) Heat transfer coefficient as a function of pressure in the strip, from Eq. [13] with $h_{\min} = 8.5$ kW/m^{2}K (Color figure online).

begins with an initial estimate, which is then updated sequentially: First for the velocity in the strip; then the strip temperatures; and finally the roll temperature field. Let us call the putative solution in the strip at iteration i $(\mathbf{v}^i, T^i)$, and designate the solution obtained using that iterate $(\mathbf{v}^*, T^*)$. The next iterate is obtained by successive substitution with relaxation

$$\begin{aligned} \mathbf{v}^{i+1} &= \epsilon_r \mathbf{v}^i + (1-\epsilon_r)\mathbf{v}^* \\ T^{i+1} &= \epsilon_r T^i + (1-\epsilon_r)T^* \end{aligned} \qquad [14]$$

Typically, $\epsilon_r = 0.85$. The solution process cycles until the strip and roll shell temperatures and velocities converge according to

$$\frac{\|\mathbf{v}^* - \mathbf{v}^{\mathbf{i}}\|}{\|\mathbf{v}^*\|} \le \epsilon_v \quad \text{and} \quad \frac{\max|T^* - T^i|}{\|T^*\|} \le \epsilon_T, \qquad [15]$$

where $\|\cdot\|$ indicates the L_2 norm. In the simulations reported in the next sections, both ϵ_v and ϵ_T are set equal to 5×10^{-4}. The maximum nodal deviation in temperature is used instead of the L_2 norm because the highly non-linear nature of the enthalpy curve can lead to significant local deviations near the solidification front, which are important to us, whereas the L_2 norm can mask those deviations when averaging over a large domain where most of the solution is not changing.

When solving for the velocity in the strip, pressure is eliminated from the equations by modifying Eq. [3] to allow a small artificial compressibility[23]

$$\nabla \cdot \mathbf{v} = -\epsilon_p p, \qquad [16]$$

where ϵ_p is called a penalty parameter, set to 10^{-5} for all of the examples in this paper. This simplifies the solution of Eq. [4] by eliminating the pressure, which is then recovered from the velocity solution using Eq. [16].

The velocities can be rather high in the inlet, where they are of less interest to us for this work. For this reason, the liquid viscosity μ_ℓ is made somewhat higher than the physical value, typically 2.5×10^{-3} MPa s. The results of interest to our prediction of microstructure and texture are not very sensitive to this value. After the velocity solution has been obtained as just described, the pressure solution from the strip velocity calculation is used to compute $h(p)$. The temperature solution in the strip is then computed by solving Eq. [5].

Finally, the temperature solution in the rolls is computed using Eq. [7]. The temperatures in the strip and rolls are solved sequentially for computational efficiency. Please note that at each iteration, the latest values from each domain are used to apply the boundary condition of Eq. [1], and thus the velocity, pressure, and strip and roll temperatures are all fully coupled when convergence is achieved. To further improve computational efficiency, most of the conductance and advection matrices in the rolls are saved after the first iteration, because they never change, and only the boundary condition contributions to the matrices and force vector are updated on subsequent iterations.

All of the simulations included in this article used topologically equivalent grids. This enables the use of solutions for problems having different parameters or dimensions to be used as initial conditions for other simulations. Grid-converged solutions were obtained with the mesh in the strip having $211 \times 41 = 8651$ nodes, graded toward the strip–roll interface, and each roll having $242 \times 21 = 5082$ nodes, also graded toward the strip–roll interface. The total number of grid points is thus 19,115. Increasing the strip mesh density to 313×61 nodes resulted in changes of less than 1 pct in the temperature and pressure fields, and thus also the separating force, forward slip, and exit temperature. The grid points for the strip and roll coincide at the boundary for ease of implementing the boundary conditions (see Figure 3). One complete iteration for velocity and temperature takes about 1.7 cpu seconds on 2020 Macbook Air with M1 chipset. Depending on how close the initial condition is to the converged solution, the complete solution for a given set of parameters takes about 3 to 7 minutes.

A. *Predicting Microstructure and Texture*

Our ultimate goal is to predict microstructure and texture in the cast strip. To that end, we begin by extracting streamlines in the strip in post-processing by introducing particles at locations of interest through the thickness at the roll nip, and integrating backward toward the inlet until the coherency point is reached. We then reverse the direction, starting at the coherency point, and record the velocity gradient history along each streamline. Extracting the streamline data in this fashion ensures that their final positions at the roll nip coincide with our locations of interest.

The velocity gradient history for each streamline is passed to the VPSC (Viscoplastic Self-Consistent) code[24] for further processing. In VPSC, the velocity gradient is decomposed into the translation gradient **L**, deformation gradient **F**, and rotational **R** components. The final deformation gradient, which relates the initial crystal morphology at the coherency point to the final morphology at the roll nip, is obtained by integrating its incremental value along the streamline. Since the AA1050 melt is highly grain refined, following Forbord *et al.*[1] and Rodrigues *et al.*,[13,14] we assume that the initial microstructure consists of randomly oriented, spherical equiaxed grains. Thus, any coordinate $\boldsymbol{X}$ on the undeformed initial grain surface satisfies

$$\boldsymbol{X} \cdot \boldsymbol{X} = 1. \qquad [17]$$

The corresponding points $\boldsymbol{x}$ on the deformed crystal then satisfy

$$\left(\mathbf{F} \cdot \mathbf{F}^{\mathbf{T}}\right)^{-1}_{jk} x_j x_k = 1. \qquad [18]$$

Equation [18] is the general equation of an ellipsoid. The square root of the eigenvalues of $\left(\mathbf{F} \cdot \mathbf{F}^{\mathbf{T}}\right)$ correspond to the lengths of the axes of the ellipsoid, and the eigenvectors define its principal directions.[25] Although the calculation is done in 3-D, since we consider the strip to be in plane strain, the eigenvalue corresponding to the eigenvector in the cross-strip direction is always equal to one, and the grain takes on the shape of an ellipse in the longitudinal plane formed by the casting and through-thickness directions. The aspect ratio of this ellipse is equal to the ratio of the largest to smallest eigenvalue, and the ellipse is inclined to the casting direction by the angle between the casting centerline and the principal axis corresponding to the largest eigenvalue. We will use these two parameters, *i.e.*, the grain aspect ratio and its inclination angle to characterize the microstructure.

The rotational component contains the information needed to compute the rotation of the crystal axes for each grain during deformation. The details of this calculation are somewhat more complicated, and well documented in the literature, so we leave the details to the interested reader.[24,25] The microstructure and crystallographic texture are evolved along each streamline by introducing 1000 randomly oriented equiaxed grains at the coherency point, and then integrating their evolution along the streamline to the roll nip. The final crystallographic orientation of each grain is placed on a stereographic projection to create a pole figure, and we also record the grain aspect ratio and inclination angle. The results of these calculations will be compared to measured microstructure data from the cast strip in the next section.

IV. MODEL VALIDATION

The model was applied to analyze AA1050 cast in an industrial Fata-Hunter caster during production. The caster was operated in "gap mode," meaning that the distance between the rolls is set, and the separating force and forward slip are outcomes generated by the solidification characteristics and associated casting parameters.

There were two phases to this study. In the "Training" phase, the model parameters that gave the best fit to measured values in a production run at Assan Aluminum for the separating force, strip exit speed, and microstructure parameters (grain aspect ratios and inclination angles through the strip thickness) were determined.

In a second "Validation" phase, the model was applied to a different production run on the same caster. In the validation trial, several different strip thicknesses were produced under a variety of conditions, including changes to the roll speed and caster setup. In the validation trial, we also measured through-thickness crystallographic textures, and compared them to the computed textures from the model.

In both the training and validation phases, the cast strip in both phases was 2230 mm width and the inlet height $t_{\text{in}} = 3$ mm. The meniscus parameters were set to $R_{\text{free}} = 8$ mm, and $Lx_{\text{free}} = 5$ mm, and the slip coefficient was set to 30 MPa/mm/s for all cases. The remaining salient production data are given in Table III. To conserve space, we have also included in the table the computed results for strip exit speed and separating force obtained in the simulations described in the next sections.

A. *Training Trial*

Figure 6(b) shows a longitudinal micrograph from the middle of the strip, prepared by mechanical polishing and electrochemical etching in Barker's reagent, viewed in polarized light to colorize the grains. The less-deformed inner core and outer highly sheared layers are evident in the micrograph. We characterize the microstructure by the aspect ratio of each grain, and its inclination with respect to the strip centerline. To aid in determining these characteristics from the micrograph, the boundary of each grain in the micrograph was first traced to highlight its boundaries. About 2000 grains are identifiable in the micrograph. This enhanced image is then imported into *ImageJ*,[26] and two different methods are applied to obtain the aspect ratio and inclination angle for each grain. In what we call the "Ellipse method," an ellipse is fit to each grain. The aspect ratio of the grain in this method is the ratio of the major to minor axes of the ellipse, and the inclination

angle is the angle between the ellipse major axis and the casting axis.

We also used the "Feret caliper method" to compute these same quantities. The maximum and minimum caliper, $F_c^{\max}$ and $F_c^{\min}$, are defined as the longest and shortest distance, respectively, between the two parallel planes restricting the grain perpendicular to that direction. The aspect ratio in the Feret method is defined as $F_c^{\max}/F_c^{\min}$, and the inclination angle is the angle between the maximum caliper and the casting axis. The measurement results were very similar using both methods, and we chose to include here the results using the Ellipse method.

The scatter plots in Figures 6(a) and (c) include the 998 grains in the micrograph whose area is larger than 1000 μm^2. Each dot in the scatter plot represents one grain, and the diameter of the dot is scaled by its respective area in the micrograph. The scatter in the grain data is due mostly to variations among the grains, rather than errors in the measurements. Note that it was difficult to distinguish the grains very close to the surface, so the measurements become more sparse and have a wider range as they approach the top and bottom surfaces, which are indicated by horizontal dashed lines. We were unable to resolve grains closer than 500 to 600 μm to the surfaces. The solid red curves in Figures 6(a) and (c) show the results from the TRC model, which we describe next.

Table III. Some of the Important Process Data for the Training and Validation Datasets

Plant Data	Training	Validation		
Strip Gage [mm]	5.13	5.19	4.68	4.27
R_{TOP} [mm]	527.3	527.75	527.75	527.75
R_{BOT} [mm]	526.5	525.75	525.75	525.75
T_w [K]	332.7	323.5	323.4	323.0
Roll Gap [mm]	4.99	4.65	3.94	3.33
$x_{setback}$ [mm]	67.0	65.8	63.0	61.1
$y_{setback}$ [mm]	0.5	0.1	0.0	0.0
V_{roll} [mm/s]	26.67	26.5	30.0	32.33
T_{inlet} [K]	966.9	965.7	966.7	966.7
V_{exit} [mm/s]	29.17	29.0	33.33	35.83
V_{exit} [mm/s] (Model)	28.9	28.8	32.6	35.13
Separating Force [MN]	11.15	11.96	12.91	14.10
Separating Force [MN] (model)	11.53	12.49	13.49	13.94

The training case was modeled using the computational methods described in Section 2. Many simulations were run covering a wide range of parameter space, with the goal of matching as many of the experimental observations as closely as possible. We found that there were many combinations of parameters that could match some of the process data (*e.g.*, the roll separating force and forward slip). However, the window in parameter space became much narrower when we also included the microstructure features.

Of particular note is the value for h_{min}. Careful examination of Figure 6(a) shows asymmetry of the angles on the top and bottom halves of the strip. We were able to reproduce that asymmetry by setting $[h_{min}^{top}, h_{min}^{bot}] = [8.5, 7.5]$ W/mm^{2}K. This clearly illustrates the sensitivity of the strip response to the heat transfer conditions. We will return to this point when we discuss the validation trial below, and again in the discussion.

Figure 7(a) shows the temperature field in the strip and part of the steel roll shells, along with a sampling of the streamlines in the strip used to extract the velocity gradient histories for VPSC. We also show the isopleths $g_s = (0.995,\ 0.57,\ 0.005)$, representing the locations of the liquidus, coherency temperature, and solidus in the

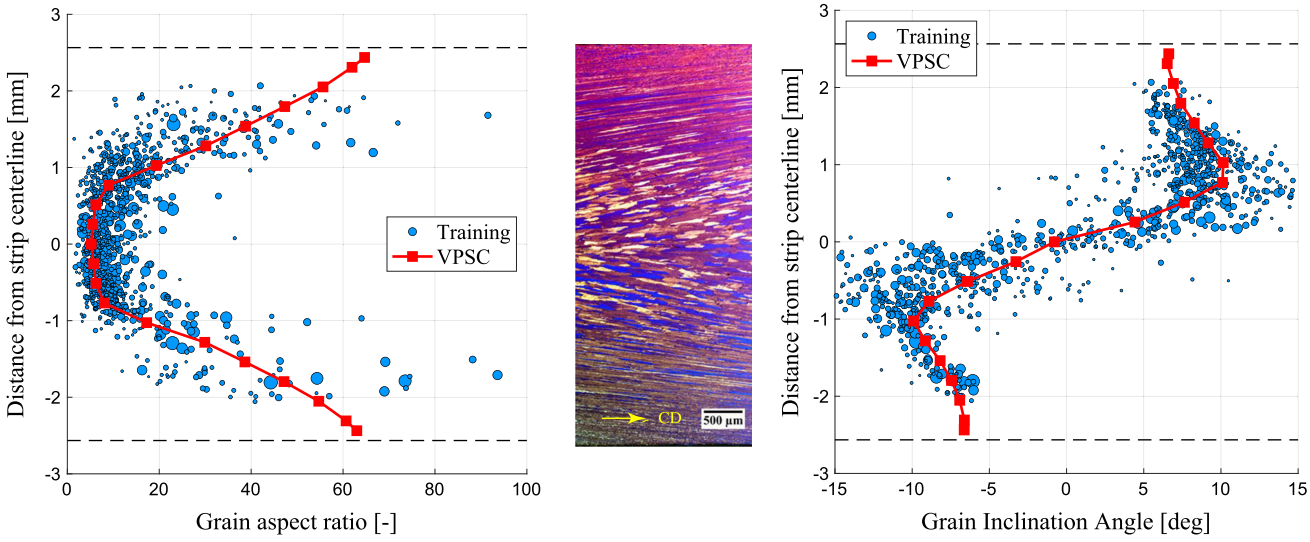

(a) Aspect ratios **(b)** Micrograph **(c)** Inclination angles

Fig. 6—Microstructure of the training set. (*a*) Grain aspect ratios; (*b*) Optical micrograph, scaled to the strip width in the graphs in (a) and (*c*); (c) Grain inclination angles. Data points in (a) and (c) are scaled by their area in the micrograph. The red curves show the model results for the training case. CD indicates the casting direction (Color figure online).

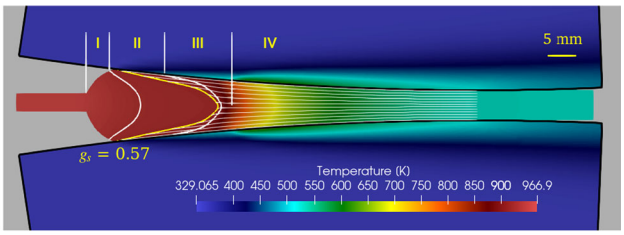

(a) Temperatures, streamlines and isotherms

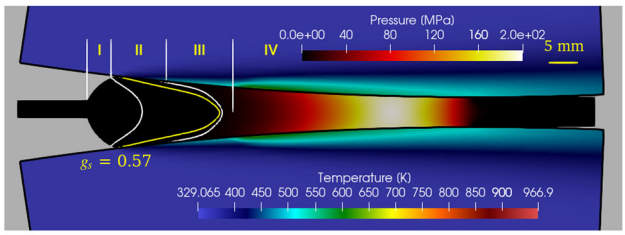

(b) Strip pressure and roll temperatures

Fig. 7—Model results for the training case. (*a*) Temperatures, streamlines, and the solidus, coherency, and liquidus curves. (*b*) Pressure in the strip and temperature in the rolls. Regions I–IV correspond to those in Fig. 1(*c*) (Color figure online).

strip. The temperature in the rolls increases sharply just past the final solidification point at the centerline, corresponding to the rapid increase in the heat transfer coefficient associated with the ability of the solid to support increasing pressure. This is illustrated more clearly in Figure 7(b), which shows the pressure in the strip, along with the temperatures in the rolls near the strip.

We can associate the locations in the simulated strip corresponding to Regions I to IV in Figure 1. Region I is the meniscus, and the length on the surface between the liquidus and solidus is Region II. The next portion of the strip, between the end of the solidus on the surface and the point where $P = P_{\text{mid}}$ at the strip centerline cannot support significant pressure due to the semi-solid interior. This corresponds to Region III. The remaining portion of the strip extending out to the roll nip is then Region IV. This demonstrates that the pressure-dependent heat transfer coefficient is able to capture, at least qualitatively, the features observed by Forbord *et al.*[1]

We next apply the procedure described in Section III–A to compute the microstructure and texture using VPSC. The computed grain aspect ratios and grain inclination angles for this case are shown in Figures 6(a) and (c), respectively, along with the microstructure characteristics of the cast strip, measured using the Ellipse method. The values for the roll separating force and exit speed are given in Table III, where it can be seen that the model predictions are within 5 pct or less compared to the measured values. The agreement between the computed and measured microstructure features and process data is quite satisfactory.

Figure 8 shows simulated {111} pole figures representing the crystallographic texture through the thickness of the strip. The mid-plane of the strip (t/2) shows a plane strain compression texture typical of rolled aluminum. The computed textures are nearly mirror images across the centerline. The plane strain compression texture rotates about the transverse direction (TD) away from the casting direction (CD) as the location approaches the surface. Close to the surface, there is a transition to 45 deg ND-rotated cube shear texture, corresponding to the region of high shear. The location of the transition between the interior plane strain compression and surface shear textures, shown in Figures 8(b) and (f), is slightly different near the top and bottom surfaces, owing to the small asymmetry in the respective values of h_{min} at the top and bottom roll–strip interfaces. Texture measurements were not available for this trial, so further comparisons will be delayed to the validation trial, in the next section.

B. *Validation Trial*

The results shown thus far are encouraging. In order to validate the model, we also need to further examine several aspects: (1) the process should be sufficiently reproducible that similar casting conditions produce similar results in different trials; (2) variations in processing conditions, such as changes in casting speed, strip thickness, and inlet configuration can be modeled without resorting to complete recalibration of the model parameters; and (3) the accuracy of the texture measurements needs to verified.

To that end, a second plant trial was conducted. The beginning of the production run for this trial was at approximately the same gage (5.19 mm) as that of the training trial. Later, the gage was reduced twice, first to 4.68 mm, then to 4.27 mm. Each gage change was accompanied by changes to the roll gap, roll speed, and to the offset of the inlet corresponding to standard operating practices for each gage. These changes were made "on the fly" without stopping and restarting the caster. See Table III for the details. The samples taken for analysis from each gage were obtained from strip produced after sufficient time had elapsed under the new conditions to ensure that steady-state conditions had been established.

Figure 9 displays micrographs of longitudinal samples from the three gages in the validation trial. These samples were prepared and analyzed in the same manner as described for the training set. The similarity of these the micrographs to the one from the training trial (Figure 6(b)) is evident, and there is no need to repeat the description.

The modeling for the three validation gages was conducted exactly as described for the training case, with one exception. Notice in Table III that the measured separating force for the 5.19 mm strip in the validation case is about 7 pct higher than for the 5.13 mm gage in the training case. The inlet setback was also smaller for this gage in the validation trial. The larger gage and smaller setback should make the separating force *smaller* for the 5.19 mm strip compared to the training set, rather than larger. There were also some very small differences in the roll diameters and water

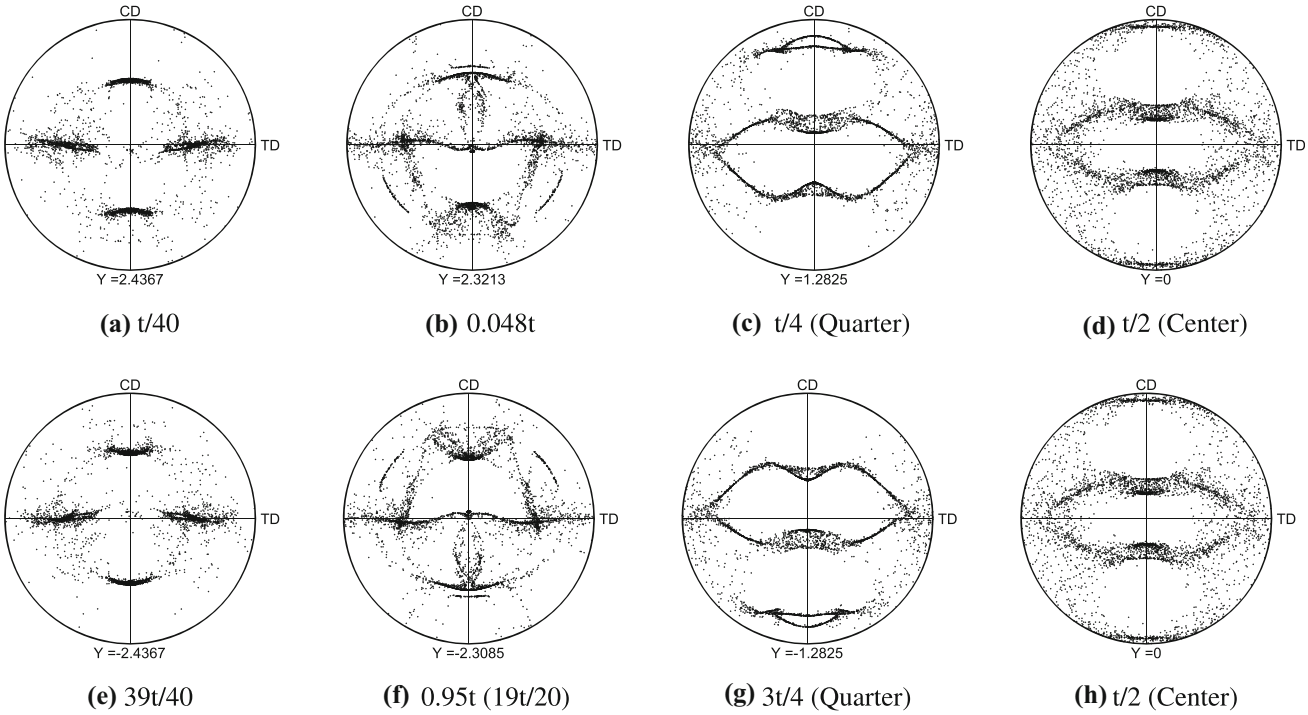

(a) t/40 **(b)** 0.048t **(c)** t/4 (Quarter) **(d)** t/2 (Center)

(e) 39t/40 **(f)** 0.95t (19t/20) **(g)** 3t/4 (Quarter) **(h)** t/2 (Center)

Fig. 8—Computed {111} pole figures through the 5.13 mm strip, above (top) and below (bottom) the centerline. CD indicates the casting direction, and TD the transverse direction in the strip.

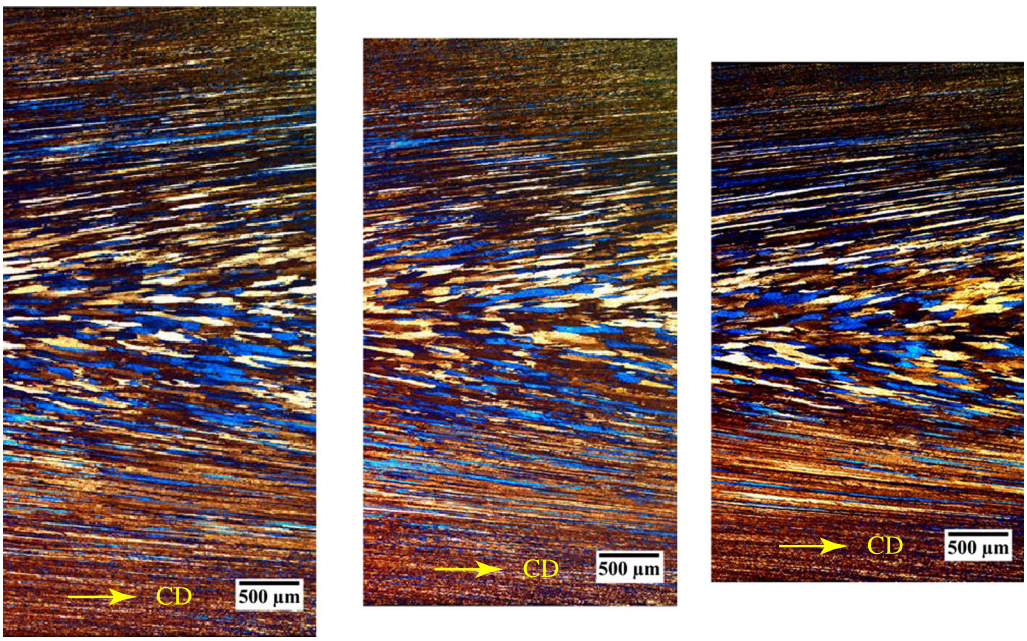

(a) 5.19 mm strip **(b)** 4.68 mm strip **(c)** 4.27 mm strip

Fig. 9—Longitudinal micrographs of the three strip gages produced in the validation trial. CD indicates the casting direction (Color figure online).

temperatures, but these differences are not sufficient to account for the change in separating force.

We attribute the increase in separating force to improved heat transfer in the validation trial, compared to the training trial, probably due to a difference in application of the release agent, which is controlled by the operator. The roll gap setting was also smaller in the validation trial. Accordingly, the minimum heat transfer coefficients used for all gages in the validation trial were increased to $\left[h_{\min}^{\text{top}}, h_{\min}^{\text{bot}}\right] = [9.5, 9.5]$. All of the other

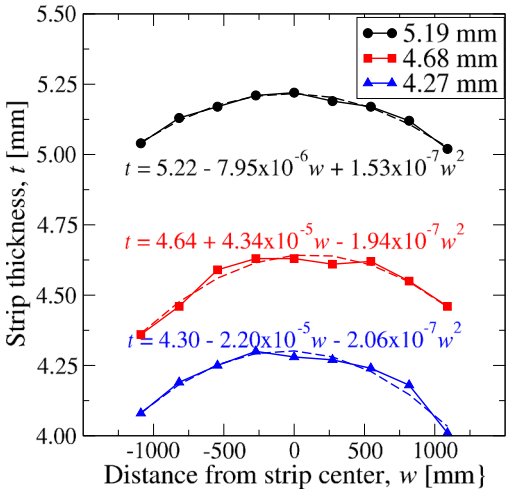

Fig. 10—Variation of the transverse strip thickness for the three strip gages in the validation trial (Color figure online).

material parameters were the same as in the validation set.

There is one other contribution to the separating force that needs to be accounted for. The simulations are 2-D, plane strain, and the microstructure analysis is done on a sample from the middle of the strip width. The rolls are very wide, and the roll gap is set by forces applied at the ends of the rolls. Thus, the rolls are subject to bending and flattening that affects the local strip thickness. The measured strip thicknesses across the strip width for the three gages in the validation trial are shown in Figure 10.

Note that during production, the outer 25 mm of the strip on each side is trimmed, so the thickness measurements were made on strip that was 2180 mm wide, whereas the cast strip is 2230 mm. For each gage, the cross-strip width was fit by a parabola, as shown in Figure 10, which was then used to extrapolate the width on both ends to account for the additional strip width. Simulations were performed at 11 thicknesses across the strip, and the total separating force was then obtained by integrating the individual 2-D values across the width. These are the values reported in Table III. The model once again predicts the separating force and forward slip for all three gages in the trial within less than 5 pct of the measured values. We note that the outermost edges of the strip are not in plane strain, but we expect that the error introduced in the separating force calculation by treating them as such is negligible, since they represent just 2 pct of the strip width.

We should also note that the cross-strip thickness data were not available for the training case, which had been completed several months earlier. We estimated that the profile would be similar to that of the 5.19 mm strip, displaced vertically by 0.06 mm, and used that projected profile to compute the separating force for the validation case. Discussion of that correction was delayed until now in order to provide the appropriate context.

The computational solutions for the three validation cases proceeded similarly to that of the training case. The figures corresponding to those of Figure 7 have been omitted here. We focus our attention on the microstructure and texture predictions instead. Figure 11 compares the computed and measured grain aspect ratios and grain inclination angles for the three cases. There are 1065, 1181, and 1197 grains, respectively, in the figure for the 5.19 mm, 4.68 mm, and 4.27 mm strip gages.

The agreement between the computed and measured microstructure features is again quite remarkable. The grain inclination angles vary only modestly among the three gages, whereas the grain aspect ratio increases significantly as the gage decreases. The core region of less-deformed material becomes narrower and the aspect ratios of the highly sheared outer regions increase as the thickness decreases.

Samples for X-ray analysis at various depths for each strip thickness were prepared by grinding to the desired depth with sandpapers and polishing with diamond and colloidal silica suspensions. Pole figure analyses were conducted on these samples using CuK_{α} radiation with Schulz apparatus on a Rigaku X-ray Diffractometer at a generator voltage and current of 40 kV and 30 mA, respectively. Incomplete {111} pole figures were obtained up to a maximum tilt angle of 75 deg. In view of the similarity of the microstructures in the upper and lower halves of the strip, the texture measurements were done only on the upper half of the strip.

Figure 12 compares the measured and computed textures for all of the strip thicknesses. The measured pole figures are shown as contour plots of reflected X-ray intensity. The model-computed textures are superimposed on the corresponding contour plots using a black dot for each grain in the simulation. The dashed circle indicates the 75 deg maximum tilt angle in the experimental measurements. For each thickness, pole figures are shown at three depths from the top surface: at approximately t/25, t/4, and t/2, from left to right. The exact depth of each pole figure is indicated under each figure, along with the strip thickness. Note that for the computed textures, streamlines were placed at the positions corresponding to the exact locations of the measured textures.

The agreement between the measured and computed textures is excellent. The computed and measured pole figures capture the core plane strain compression texture at $t/2$, its rotation toward the surface shear texture at $t/4$, and the 45 deg ND-rotated cube shear texture at the surface. This completes the model validation, demonstrating that it correctly predicts both the extrinsic measures (separating force and forward slip), as well as the intrinsic measures (microstructure and crystallographic texture) in the cast strip.

V. APPLYING THE VALIDATED MODEL

The microstructural features and crystallographic textures in the training and validation datasets do not show a great deal of variation, due to the selection of

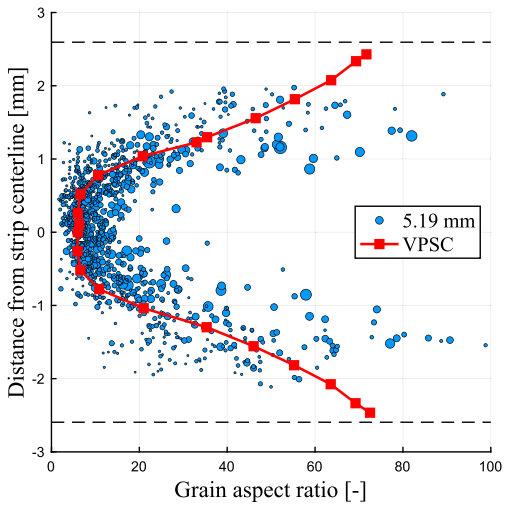

(a) 5.19 mm strip

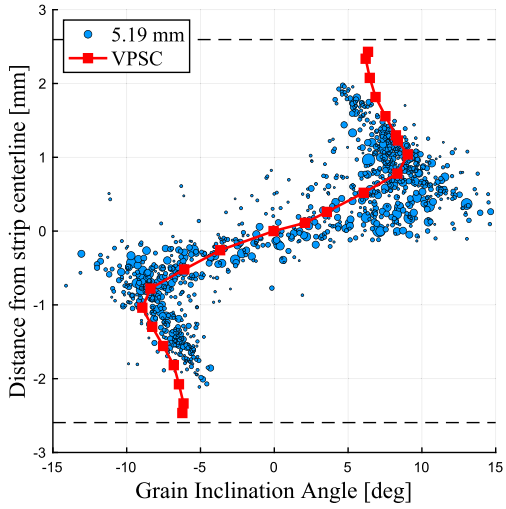

(b) 5.19 mm strip

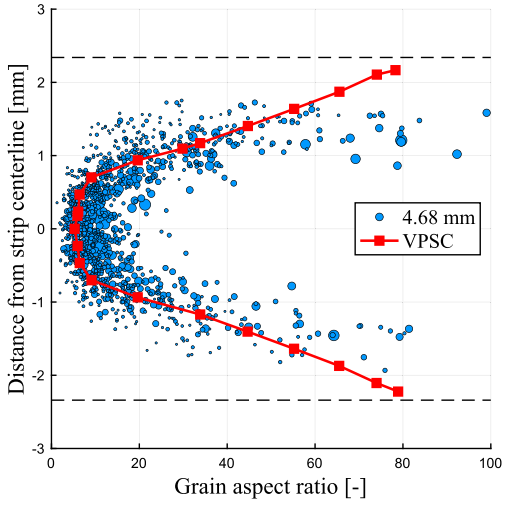

(c) 4.68 mm strip

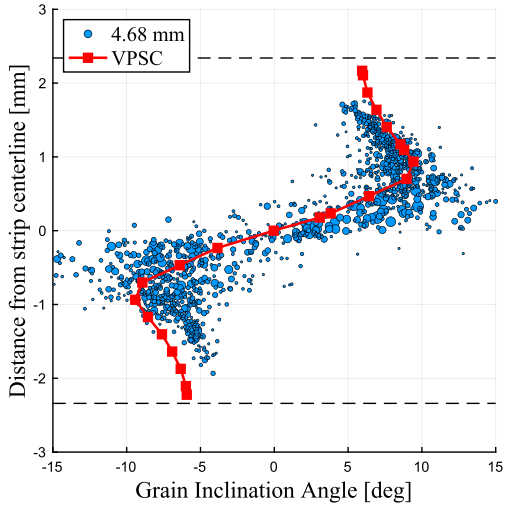

(d) 4.68 mm strip

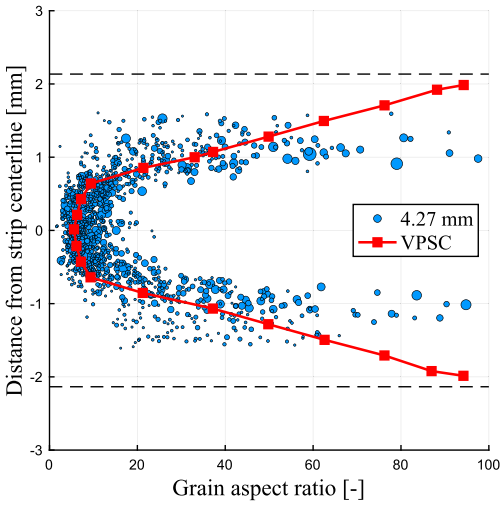

(e) 4.27 mm strip

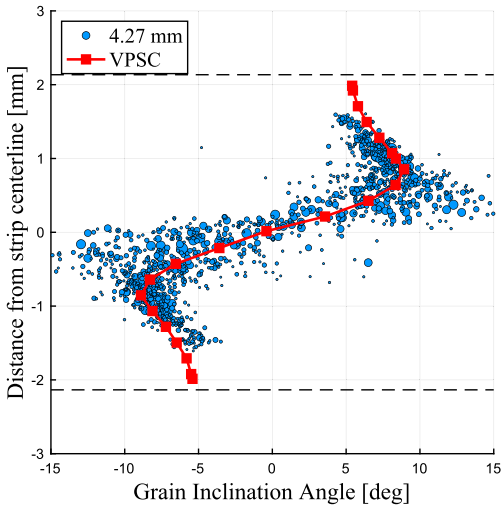

(f) 4.27 mm strip

Fig. 11—Comparison of computed and measured grain aspect ratios (left column) and grain inclination angles (right column) for three different strip thicknesses in the validation trial (Color figure online).

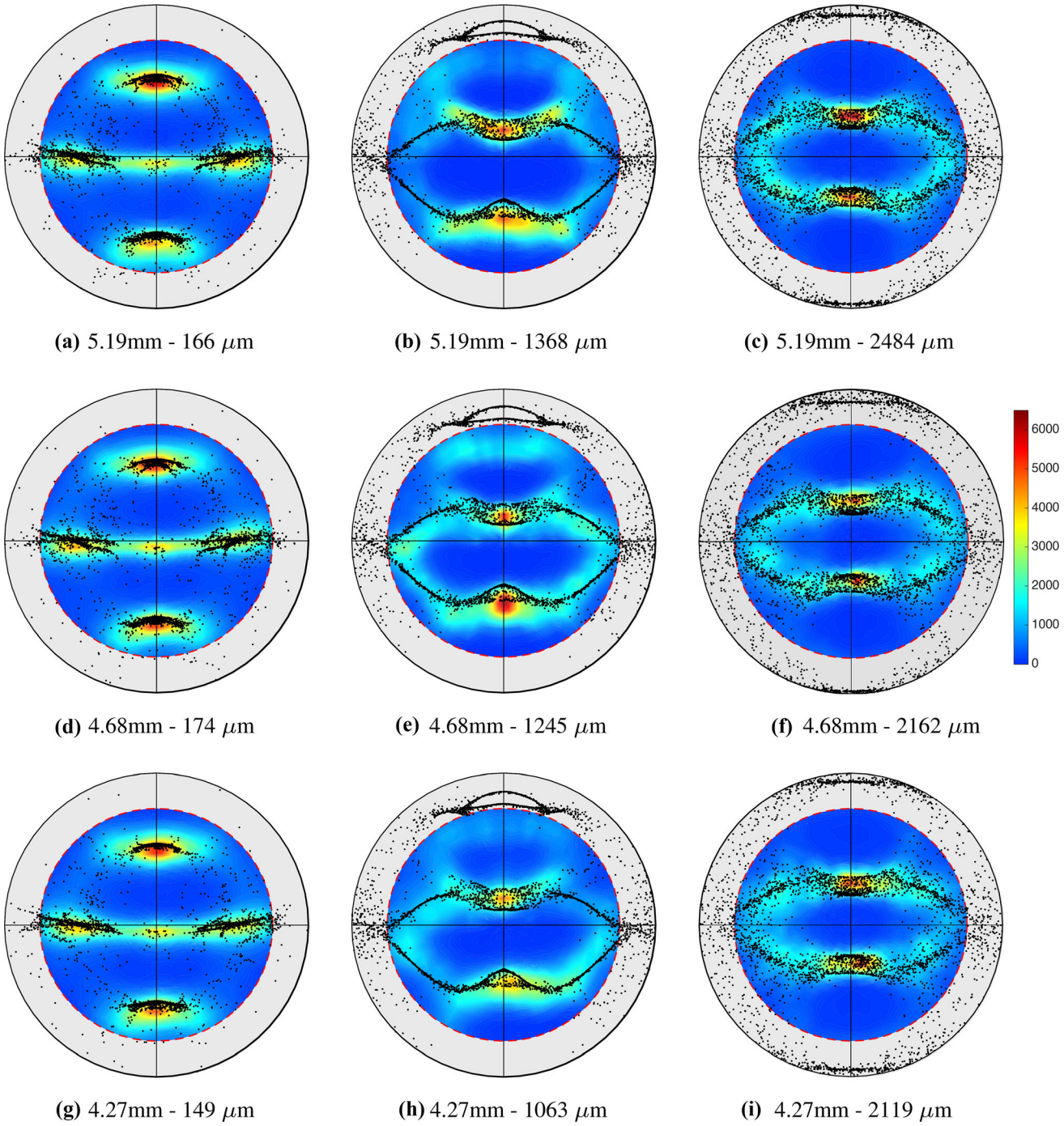

Fig. 12—Comparison of measured and computed {111} pole figures through the strips in the validation trial. (*a*)–(*c*) 5.19 mm strip; (*d*)–(*f*) 4.68 mm strip; (*g*)–(*i*) 4.27 mm strip at approximately $t/25$, $t/4$, and $t/2$, left to right. The casting direction is to the north, and transverse direction to the east in each pole figure (Color figure online).

production practices intended to produce consistent products. In this section, we explore variations in processing and caster design practices to alter the cast microstructure. In particular we will consider changes in horizontal setback of the inlet from the roll nip; roll speed; incoming metal temperature; and caster roll shell material composition. Exploring parameter space computationally represents the essential value of a validated model. We chose the 5.19-mm-thick strip from the validation dataset as the base case for variations in the parameters, and in the sections that follow, only one process parameter varies while the rest remain the same as in the base case.

It should be noted that varying each of these parameters can be significantly easier to do in simulation than in practice. Physical limitation of the space between the rolls and geometry of the inlet may limit the horizontal setback. The ability to supply sufficient

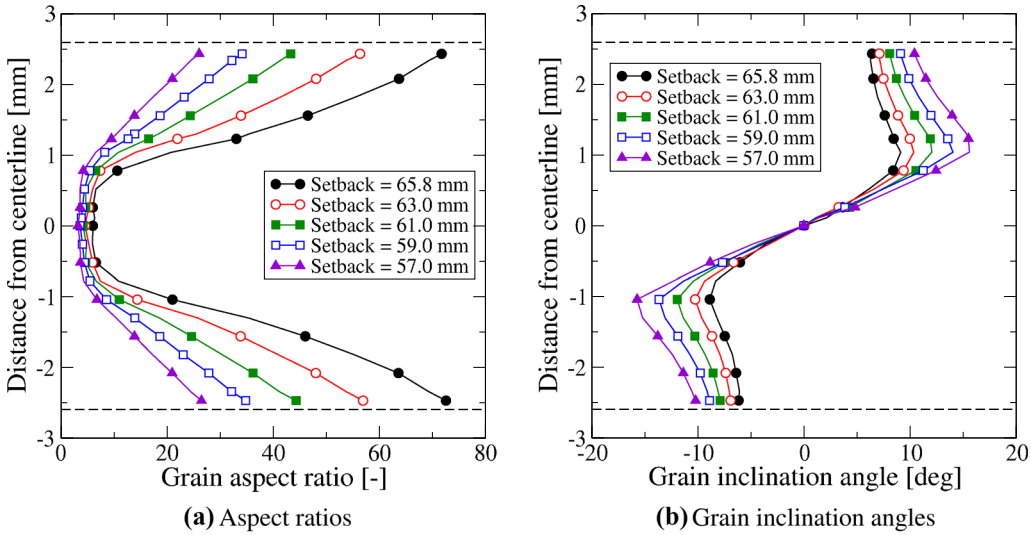

Fig. 13—Computed microstructural features for various values of the inlet horizontal setback. (*a*) Grain aspect ratios and (*b*) grain inclination angles (Color figure online).

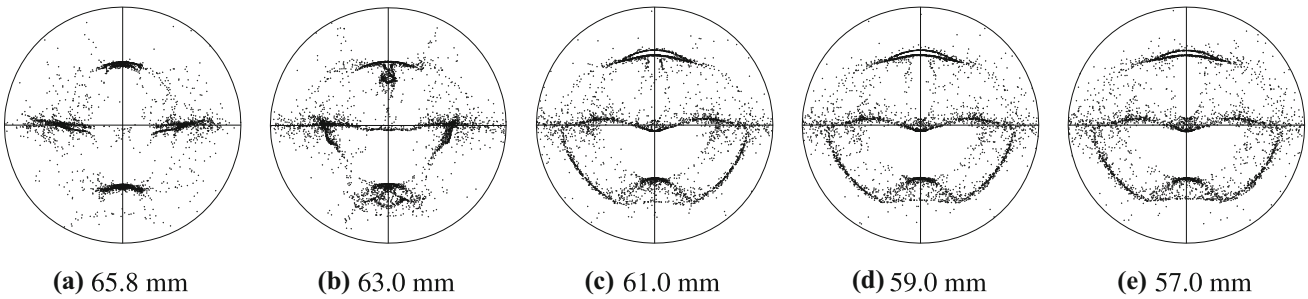

Fig. 14—Computed near-surface textures ($t - 166$ μm) for various values of the inlet horizontal setback. (*a*) 65.8 mm, (*b*) 63 mm, (*c*) 61 mm, (*d*) 59 mm, and (*e*) 57 mm.

molten alloy through the inlet may limit the roll speed, and increasing the incoming metal temperature can produce deleterious effects on melt quality. Switching to copper roll shells may lead to high separation forces that exceed the caster capabilities. Nevertheless, the results presented below give a strong indication that the cast microstructure can be controlled by these variations, and provide guidance to product and process designers.

A. *Inlet Horizontal Setback*

The base case strip shows a highly deformed grain structure and strong shear texture at the surface. (See Figures 9(a), 11(a) and (b), and 12(a).) Previous studies in 8006 alloys[27] have shown that reducing the horizontal setback leads to less-deformed surface structures, which are also associated with improved formability of the cast strip after annealing. Accordingly, we considered several different reduced setback distances compared to 65.8 mm in the base case: 63, 61, 59, and 57 mm. The results for the computed microstructure features are summarized in Figures 13(a) and (b), and the corresponding near-surface textures are shown in Figure 14.

The results show that reducing horizontal setback has a pronounced positive effect on the surface microstructure and texture. The grain aspect ratios in the outer portion of the strip decrease continuously, and the grain inclination angles increase continuously as the setback decreases. The near-surface texture shows a corresponding reduction in shear component, transitioning to the rotated compression texture for a setback of 61 mm. Further reduction in setback has only a modest effect on texture beyond this value, even though the microstructure continues to change. All of these features indicate that reducing the setback leads to less severe deformation.

Figure 15(a) shows the temperature profile along the centerline of the strip for various values of the setback, and Figure 15(b) shows the corresponding variation of the separating force. There are two mechanisms at work that affect the microstructure and separating force: (i) a *thermal* effect, where lower setback leads to higher temperatures in the strip, which correspond to lower viscosity; and (ii) a *mechanical* effect, caused by the fact that the strip is under the rolls for a shorter time when the setback decreases. We will be able to separate these mechanisms when we consider melt inlet temperature below.

B. *Caster Roll Speed*

The effect of caster roll speed was investigated by increasing roll speed from 26.5 mm/s in the base case to 28, 30, 32, and 34 mm/s. The resulting microstructures and textures, summarized in Figures 16 and 17, show many similarities to variation of horizontal setback. As roll speed increases, the strip runs hotter and is inside the rolls for a shorter period of time. This leads to decreasing grain aspect ratios, increasing grain inclination angles, and decreasing strength of near-surface shear texture, eventually giving way to rotated compression texture at high enough roll speed, beyond which there is little change. Figures 18(a) and (b) show that increasing caster roll speed leads to increasing temperatures along the strip centerline, and decreasing separating force.

C. *Inlet Metal Temperature*

The thermal and mechanical contributions to the changes in microstructure and separating force can be distinguished by considering changes in the incoming metal temperature. The base case had $T_{\text{inlet}} = 965.7$ K. For this part of the parameter study, we considered values for T_{inlet} of 950, 960, 970, 980 and 990 K. The results, summarized in Figures 19, 20, 21, show that metal inlet temperature has a very minor effect on the microstructure and on the strip centerline temperature compared to other parameters, but increasing T_{inlet} does reduce the separating force. We note that the increased superheat is fairly quickly dissipated in the solidification region, because the associated sensible heat is much smaller than the latent heat. See Figure 21(a). This result demonstrates that the primary mechanism for

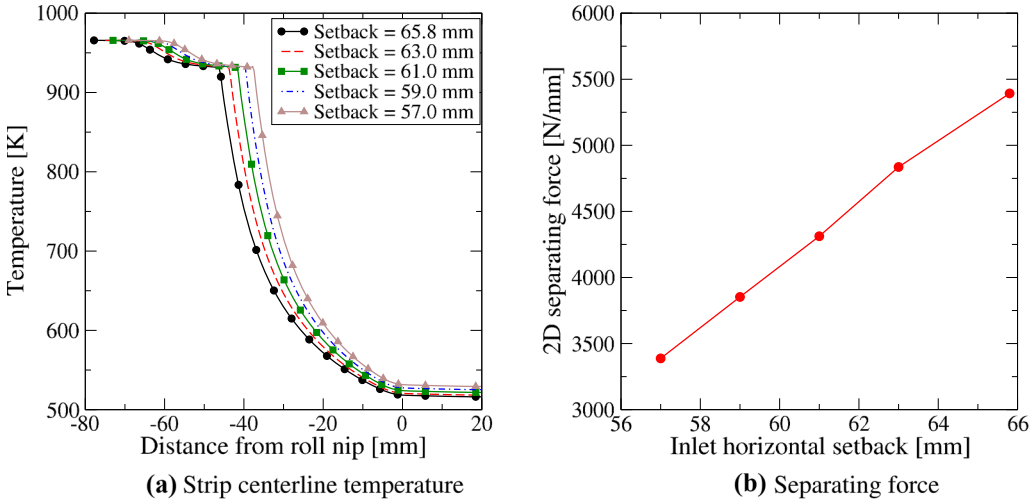

Fig. 15—Variation of computed (*a*) strip centerline temperature and (*b*) mid-strip separating force with inlet horizontal setback (Color figure online).

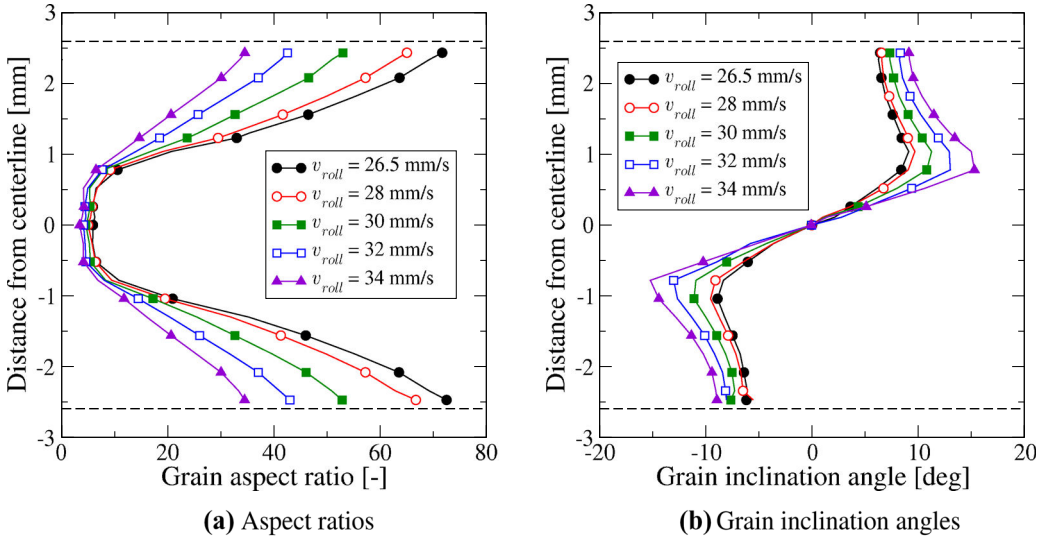

Fig. 16—Computed microstructural features for various values of the caster roll speed. (*a*) Grain aspect ratios and (*b*) grain inclination angles (Color figure online).

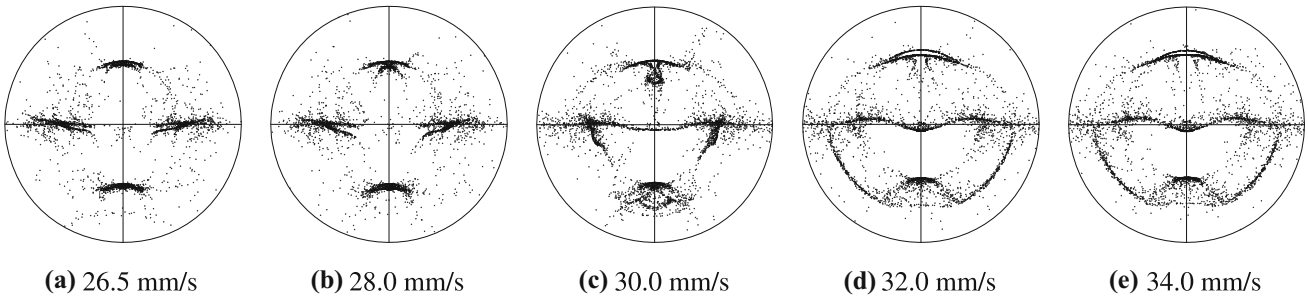

Fig. 17—Computed near-surface textures ($t - 166$ μm) for various values of the caster roll speed. (*a*) 26.5 mm/s, (*b*) 28 mm/s, (*c*) 30 mm/s, (*d*) 32 mm/s, and (*e*) 34 mm/s.

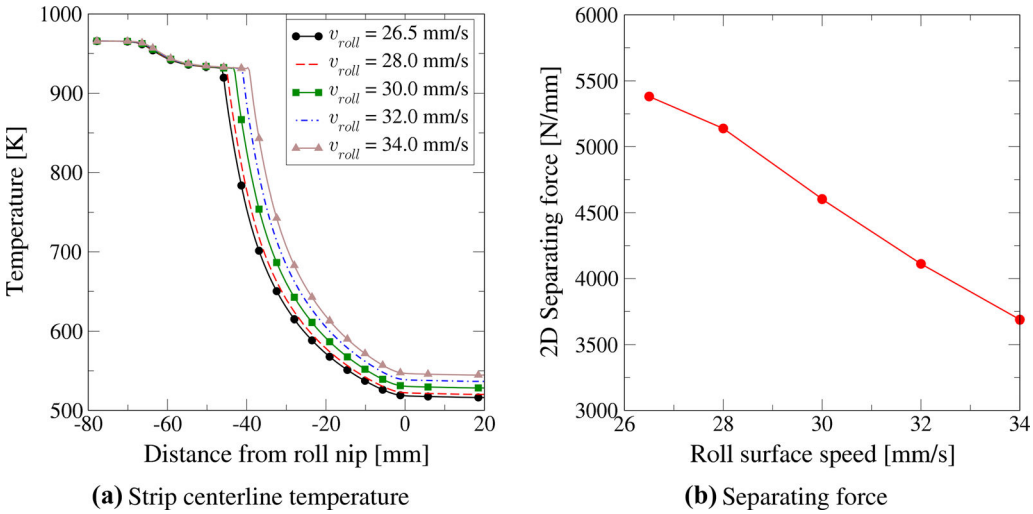

(a) Strip centerline temperature **(b)** Separating force

Fig. 18—Variation of computed (*a*) strip centerline temperatures and (*b*) mid-strip separating force with caster roll speed (Color figure online).

microstructure formation is mechanical deformation, and that thermal effects are secondary.

D. *Copper Roll Shells*

Finally, we examine the effect of substituting Cu roll shells for the steel shells that we have considered thus far. The only change in these simulations compared to the base case was to change the roll shell thermal conductivity. We repeated the roll speed variations from Section V–B for the Cu roll shells. We find that the computed microstructures are much different in character than those for the steel shell: The grain aspect ratios, shown in Figure 22(a), have a sharp kink at about $t/4$, while the grain inclination angles are not much affected by roll speed, as shown in Figure 22(b). The computed textures vary with roll speed in a similar fashion to those found for the steel shells (Figure 23).

Changing to Cu shells has a very large effect on the temperature and separating force, as shown in Figure 24. The strip exit temperatures are almost 100 K lower for the Cu roll shells than they were for the steel shells. See Figure 15(a). We should note that the computed strip temperatures are low enough that it is probably beyond the applicability of the assumption of purely viscoplastic behavior, but we can nevertheless understand the trends. Figure 24(b) compares the computed separating forces for the steel and Cu shells, where one can see that the colder strip leads to much larger separating force.

VI. DISCUSSION

Our results show that the grain structure in the central core of the strip is essentially determined by plane strain compression, and is thus only moderately sensitive to the various process parameters. On the other hand, the outer region of the strip, between the central core and the surface, is quite sensitive to those same parameters. At fixed h, increasing β increases the grain aspect ratio in the outer region, while having only a small effect on the grain inclination angles. At fixed β, the grain inclination angle is very strongly affected by h, and in particular by $h_{\min}$. Increasing $h_{\min}$ decreases the maximum inclination angle. It should be clear from this discussion that matching the separating force and the microstructural features at the same time can only be achieved in a narrow range of the parameters. We expect that the parameter set that provides good agreement with the measured strip characteristics will depend on the casting machine, and to some extent on the operator, who

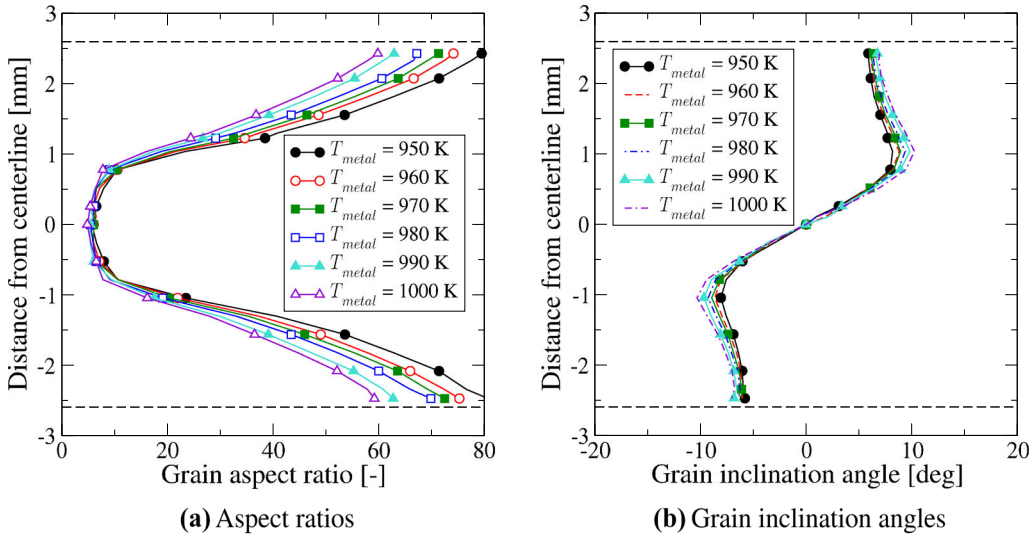

Fig. 19—Computed microstructural features for various values of the metal inlet temperature. (*a*) Grain aspect ratios and (*b*) grain inclination angles (Color figure online).

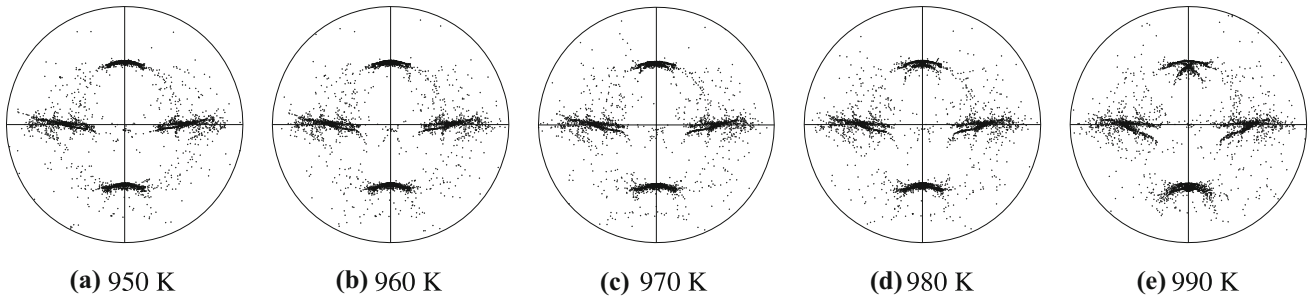

Fig. 20—Computed near-surface textures ($t - 166$ μm) for various values of the metal inlet temperature.

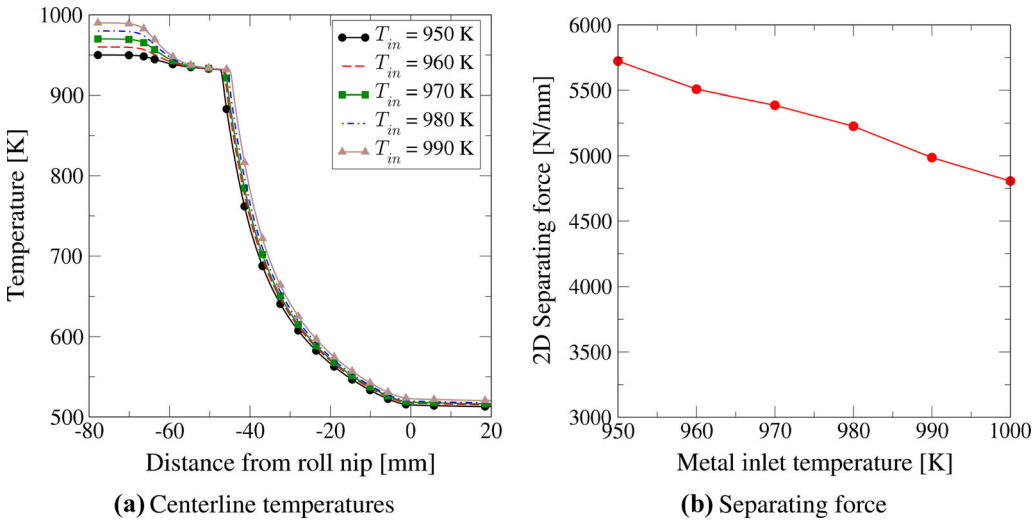

Fig. 21—Variation of computed (*a*) strip centerline temperature, (*b*) mid-strip separating force with metal inlet temperature (Color figure online).

controls the application of the release agent to ensure that the strip does not adhere to the rolls.

There are some characteristics of the casting practice for AA1050 that allow the model to work as well as it does. The melt is highly grain refined, which makes it reasonable for us to use as an initial condition randomly oriented spherical equiaxed grains. Further, there is no indication of recrystallization in the cast strip. These conditions make it relatively straightforward to use VPSC to compute the morphology and texture of the

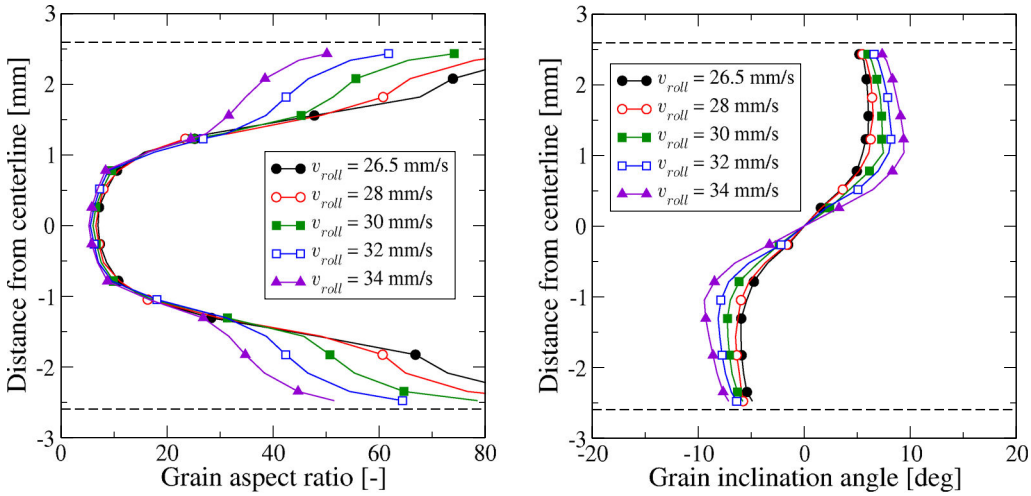

(a) Aspect ratios **(b)** Grain inclination angles

Fig. 22—Computed microstructural features for various values of the caster roll speed for Cu roll shells. (*a*) Grain aspect ratios and (*b*) grain inclination angles (Color figure online).

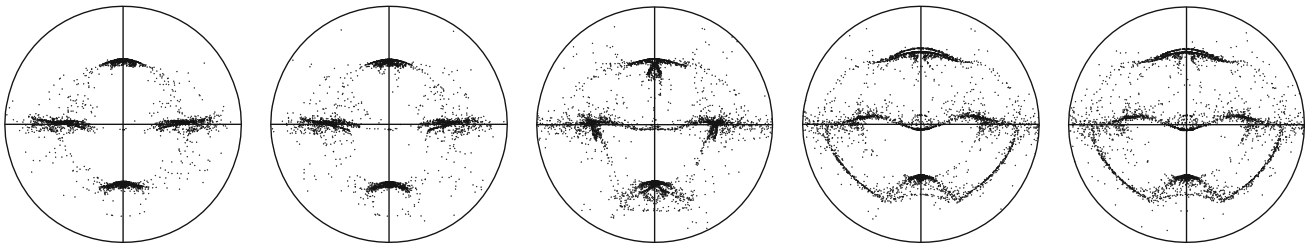

(a) 26.5 mm/s **(b)** 28.0 mm/s **(c)** 30.0 mm/s **(d)** 32.0 mm/s **(e)** 34.0 mm/s

Fig. 23—Computed near-surface textures ($t - 166$ μm) for various values of the caster roll speed for Cu roll shells. (*a*) 26.5 mm/s, (*b*) 28 mm/s, (*c*) 30 mm/s, (*d*) 32 mm/s, and (*e*) 34 mm/s.

as-cast strip. If there were no grain refinement, the initial microstructure used as input to the VPSC calculations would have to account for the columnar solidification structure. Although this is still possible, it would require significant further work to achieve.

In future work, we will consider different conditions, such as different casters with significantly different roll diameters and shell materials. We will also consider different alloys. The general methods and procedures described in this paper are expected to apply to these cases as well. The components of the model are as follows:

- Construct a geometrically accurate model of the strip and rolls;
- Provide accurate data for the thermal and mechanical properties of the alloy, including
  - Use DSC measurements to accurately represent the enthalpy–temperature curve for the alloy of interest; and
  - Determine an accurate constitutive model for the alloy, either from the literature or *via* mechanical testing.
- Specify the casting parameters (temperatures, roll speeds, *etc.*);
- Perform trials to calibrate the model roll–strip transport parameters for the new conditions

VII. SUMMARY AND CONCLUSIONS

- We consider the TRC process for AA1050 alloy in industrial practice, recording the forward slip and separating force during production. The microstructure in the strip is characterized by the aspect ratio and inclination angle of the grains.
- A model for TRC casting is developed to compute the velocity and temperature distribution in the strip and roll shells. Outputs from the model are used as inputs to VPSC to predict the microstructure and crystallographic texture of the cast strip.
- Boundary conditions for the heat and mechanical transport between the strip and roll shell are the key unknown parameters needed for the model. The

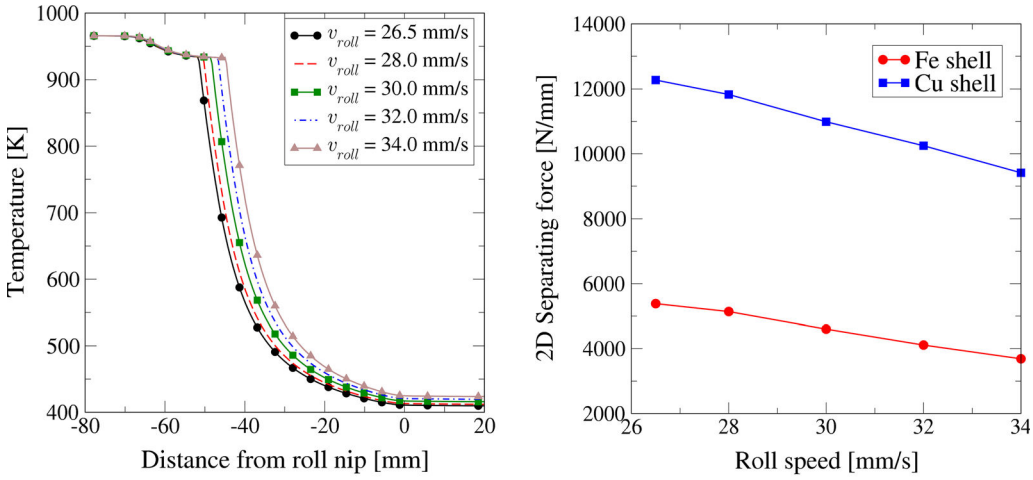

(a) Strip centerline temperature **(b)** Separating force

Fig. 24—Variation of computed (*a*) strip centerline temperatures and (*b*) mid-strip separating force with caster roll speed for Cu roll shells (Color figure online).

unknown interfacial transport parameters that provide a good fit to the forward slip, separating force, and microstructure were identified in a training trial. Material properties for the model were obtained by direct measurement (*e.g.,* by DSC) or from the literature.

- The model was then validated in a second trial, using different conditions to produce several different strip thicknesses. In this validation trial, predictions for forward slip and separating force are all within less that 5 pct of their corresponding measured values over a range of gages, casting speeds, and caster setup. The microstructure and crystallographic texture are all shown to be in excellent agreement with experimental observations.
- Variation of parameters in the validated model shows that the near-surface microstructure can be altered in a controlled way *via* process parameters such as inlet setback, caster roll speed metal inlet temperature, and roll shell composition.

ACKNOWLEDGMENTS

We are grateful to R. Lebensohn of Los Alamos National Laboratory for providing the VPSC code. We acknowledge the support of the Scientific and Technological Research Council of Turkey (TUBITAK) TEYDEB 1505 Project, Grant Number 5210011. We also wish to thank Mr. Nihat Yılmaz and Mr. Hikmet Kayaçetin, technicians of Assan Aluminum Research and Development Laboratory, for their invaluable help with metallographic studies and casting operations. We also thank Armand Beaudoin for helpful discussions.

CONFLICT OF INTEREST

On behalf of all authors, the corresponding author states that there is no conflict of interest.

LIST OF SYMBOLS

ROMAN SYMBOLS

A	Parameter in Sheppard and Jackson model for σ_{sat}, Eq. [12]
C_p	Specific heat at any point in the domain
c_p^s, c_p^ℓ	Specific heat of solid and liquid phases, respectively
$\mathbf{D}$	Rate of deformation tensor
$\mathbf{F}$	Deformation gradient tensor
$F_c^{\min}, F_c^{\max}$	Minimum and maximum Feret caliper
$g_s,\ g_\ell$	Solid fraction, liquid fraction
g_s^t, g_s^p	Coherency model parameters, Eq. [10]
H	Enthalpy
$h_{\min}, h_{\max}$	Min and max heat transfer coefficients at strip–roll interface
h_{out}	Heat transfer coefficient at strip surface after the roll nip
h_w	Heat transfer coefficient at the inner surface of the roll shell
$h(p)$	Heat transfer coefficient at the roll–strip interface
k	Thermal conductivity
$\mathbf{L}$	Translation gradient tensor
L_f	Latent heat of fusion
Lx_{free}	Length of the meniscus region after the inlet

$Lx_{\text{in}}, Lx_{\text{out}}$	Length of the inlet and outlet regions
n	Parameter in Sheppard and Jackson model for σ_{sat}, Eq. [12]
$\hat{\boldsymbol{n}}$	Normal unit vector
$P_{\text{mid}}, P_{\text{width}}$	Parameters in model for $h(p)$, Eq. [13]
p	Pressure
Q_D	Activation energy in Sheppard and Jackson model for σ_{sat}, Eq. [12]
$\mathbf{R}$	Rotational component of velocity gradient
$\mathcal{R}$	Ideal gas constant
R_i^t, R_i^b	Inner radii of roll shells
$R_{\text{top}}, R_{\text{bottom}}$	Outer radii of roll shells
r	Radial distance
T	Temperature
t_{in}, t	Height of the inlet, thickness of the strip
$\hat{\boldsymbol{t}}$	Tangent unit vector
$\mathbf{v}, \mathbf{v_n}, \mathbf{v_t}$	Velocity vector; normal and tangential components
w	Strip width measured from center in Figure 10
$\mathbf{X}$	Position vector for a point on an undeformed spherical grain
x	Position vector on a deformed grain
$x_{setback}, y_{setback}$	Position of the end of the inlet relative to the roll nip
Z	Zener–Holloman parameter, Eq. [11]

GREEK SYMBOLS

α	Parameter in Sheppard and Jackson model for σ_{sat}, Eq. [12]
β	Slip coefficient at the roll–strip interface
$\delta_{\text{top}}, \delta_{\text{bottom}}$	Thickness of the top or bottom roll shell
ϵ_p	Penalty parameter for pressure, Eq. [16]
ϵ_r	Relaxation parameter for iterative solution
ϵ_T, ϵ_v	Convergence parameters for iterative solution
$\dot{\varepsilon}$	Scalar strain rate
$\eta(g_s, T, \dot{\varepsilon})$	Viscosity of the solid, $g_s > g_s^t$
$\boldsymbol{\theta}$	Unit vector normal to radius
ρ	Density
σ_{sat}	Saturation stress for viscoplastic solid
$\tau_{r\theta}$	Shear stress in the strip at the surface
Ω_t, Ω_b	Angular velocity of the top and bottom rolls

REFERENCES

1. B. Forbord, B. Andersson, F. Ingvaldsen, O. Austevik, J. Horst, and I. Skauvik, *Mater. Sci. Eng. A*, 2006, vol. 415, pp. 12–20.
2. R. E. Roadman, H. M. Berman, and L. A. Lalli, in *Modeling of Casting and Welding Processes-II*, eds. J. A. Dantzig and J. T. Berry, TMS-AIME, Warrendale, PA, pp. 421–34.
3. S. Sahoo, *J. Metall.*, 2016, vol. 2016, pp. 1038950:1–13.
4. C.O. Hlady, J.K. Brimacombe, I.V. Samarasekera, and E.B. Hawbolt, *Metall. Mater. Trans. B*, 1995, vol. 26B, pp. 1019–27.
5. D. Wang, C. Zhou, G. Xu, and A. Huaiyuan, *J. Mater. Process. Tech.*, 2014, vol. 214, pp. 1275–84.
6. P. Jarry, D. Toitot, P.-Y. Menet, *Light Metals*, 1996, pp. 905–11.
7. S.M. Hwang, Y.H. Kang, *J. Eng. Ind.*, 1995, vol. 117, pp. 304–15.
8. S. Sahoo, A. Kumar, B. Dhindaw, and S. Ghosh, *Metall. Mater. Trans. B*, 2012, vol. 43B, pp. 915–24.
9. Y.-S. Lee, H.-W. Kim, and J.-H. Cho, *J. Mater. Process. Tech.*, 2015, vol. 218, pp. 41–56.
10. Y.-S. Lee, H.-W. Kim, J.-H. Cho, and S.-H. Chun, *Met. Mater. Int.*, 2017, vol. 23, pp. 923–29.
11. D. Mortensen, H. G. Fjaer, D. Lindholm, K. F. Karhausen, and J. S. Kvalevag, in *Light Metals*, ed. M. Hyland, TMS, Warrendale, pp. 1243–47. (2015).
12. O. Grydin, D. Mortensen, M. Neuser, D. Lindholm, H. G. Fjaer, and M. Schaper, *Light Metals*, 2022, pp. 728–34.
13. C.M.G. Rodrigues, A. Ludwig, M. Wu, A. Kharicha, and A. Vakhrushev, *Metall. Mater. Trans. B*, 2019, vol. 50B, pp. 1334–50.
14. C.M.G. Rodrigues, A. Ludwig, M. Wu, A. Kharicha, and A. Vakhrushev, *J. Mater. Process. Tech.*, 2020, vol. 286, pp. 116814:1–9.
15. C. Gras, M. Meredith, J. Hunt, *J. Mater. Process. Tech.*, 2005, vol. 169, pp. 156–63.
16. V. U. Akdoğan, C. Işiksaçan, H. M. Altuner, O. Birbaşar, and M. Günyüz, *Light Metals*, 2019, pp. 1137–41.
17. K.-H. Jung, D.-K. Kim, Y.-T. Im, and Y.-S. Lee, *Mater. Trans.*, 2013, vol. 54, pp. 769–75.
18. S.F. Harnish, H.A. Padilla, B.E. Gore, J.A. Dantzig, A.J. Beaudoin, I.M. Robertson, and H. Weiland, *Metall. Mater. Trans. A*, 2005, vol. 36A, pp. 357–70.
19. J.A. Dantzig, *Int. J. Numer. Meth. Eng.*, 1989, vol. 28, pp. 1769–85.
20. T. Sheppard, and A. Jackson, *Mater. Sci. Tech.*, 1997, vol. 13, pp. 203–09.
21. MATLAB: *Version 9.11.0.1769968 (R2021b)*, The MathWorks Inc., Natick, Massachusetts, 2021.
22. A. Brooks, and T.J.R. Hughes, *Comput. Method. Appl. Mech. Eng.*, 1982, vol. 32, pp. 199–259.
23. M.S. Engelman, R.L. Sani, P.M. Gresho, and M. Bercovier, *Int J. Numer. Meth. Fluids*, 1982, vol. 2, pp. 25–42.
24. O. Engler, M.-Y. Huh, and C.N. Tomé, *Metall. Mater. Trans. A*, 2000, vol. 31A, pp. 1299–1315.
25. C. N. Tomé, and R. A. Lebensohn, *Manual for Visco-plastic Self Consistent (VPSC)*, Los Alamos National Laboratory.
26. C.A. Schneider, W.S. Rasband, and K.W. Eliceiri, *Nat. Methods*, 2012, vol. 9, pp. 671–75.
27. C. Işiksaçan, O. Meydanoğlu, O. Birbaşar, and M. Gülver, *Light Metals*, 2018, pp. 971–75.

Publisher's Note Springer Nature remains neutral with regard to jurisdictional claims in published maps and institutional affiliations.